42nd Aerospace Sciences Meeting and Exhibit
January 5-8, 2004, Reno, NV

AIAA-2004-0561

A Computational Icing Effects Study for a Three-Dimensional Wing:
Comparison with Experimental Data and Investigation of Spanwise Variation

D. Thompson,* P. Mogili**, and S. Chalasani***
Computational Simulation and Design Center
Mississippi State University, Mississippi State, MS 39762

H. Addy† and Y. Choo†
National Aeronautics and Space Administration
Glenn Research Center, Cleveland, OH 44135

Abstract

Steady-state solutions of the Reynolds-averaged Navier-Stokes (RANS) equations were computed using the Cobalt flow solver for a constant-section, rectangular wing based on an extruded two-dimensional glaze ice shape. The one equation Spalart-Allmaras turbulence model was used. The results were compared with data obtained from a recent wind tunnel test. Computed results indicate that the steady RANS solutions do not accurately capture the recirculating region downstream of the ice accretion, even after a mesh refinement. The resulting predicted reattachment is farther downstream than indicated by the experimental data. Additionally, the solutions computed on a relatively coarse baseline mesh had detailed flow characteristics that were different from those computed on a refined mesh. However, the results predicted using the baseline mesh were conservative in the sense that they indicated a more severe reduction in lift than the results computed on the refined mesh or the experimental data. Steady RANS solutions were also computed to investigate the effects of spanwise variation in the ice shape. The spanwise variation was obtained via a blending function that merged the ice shape with the clean wing using a sinusoidal spanwise variation. For these configurations, the results predicted for the extruded shape provided conservative estimates for the performance degradation of the wing. Additionally, the spanwise variation in the ice shape and the resulting differences in the flow field details did not significantly change the location of the primary reattachment.

*Associate Professor, Department of Aerospace Engineering, Senior Member AIAA
**Graduate Student, Department of Aerospace Engineering, Student Member AIAA
***Graduate Student, Computational Engineering Program
†Aerospace Engineer, Icing Branch, Member AIAA

Introduction

There are two distinct applications related to the aircraft icing problem in which computational fluid dynamics (CFD) can play a significant role.[1] First is the prediction of ice accretion using software such as LEWICE[2] coupled with a viscous flow solver. The second application is a detailed flow field analysis to determine the effects of ice accretion on aircraft performance. We focus on the second application, "icing effects," in this paper.

Recently, numerous simulations of the flow fields associated with airfoils and wings with ice accretions have been reported for "icing effects" studies. Chung, et. al,[3] performed a CFD analysis of the ice contaminated wing surfaces of a turbo-prop aircraft. Their analysis was performed to obtain qualitative trends and to provide insight into the aerodynamics that may have led to a loss of control of the aircraft. Dunn and Loth,[4] Dunn, et. al,[5] Kumar and Loth,[6] and Pan, et. al,[7] computed the effects of simulated spanwise ice shapes on airfoil aerodynamics. Their simulations showed that for two-dimensional computations, detailed flow characteristics such as pressure distributions and reattachment lengths showed reasonable correlation with experimental data, as did integrated quantities such as lift, drag, and moment. Notable exceptions to this trend were that the agreement was degraded once the flow on the upper surface was fully separated and that the maximum lift values were not well predicted. In all cases mentioned above, the steady Reynolds averaged Navier-Stokes (RANS) equations were solved to compute the flow field. Kumar and Loth[8] performed two- and three-dimensional detached eddy simulations (DES) for iced airfoil/wing configurations. The agreement of time-averaged results with experimental data showed some improvement when compared to steady RANS computations.

Although computational fluid dynamics tools have made great strides in recent years, there are several unanswered questions regarding their capabilities for predicting the flow around wings with ice accretions.

The ability of geometry/mesh generation tools to adequately address the unique needs of an iced wing flow simulation is also much in question. There are significant issues related to the iced wing surface modeling including questions regarding the quality of a nonuniform rational b-spline (NURBS) representation of the surface. Additionally, within the constraints of accuracy, efficiency, and flexibility, questions remain as to what type of mesh is appropriate for a complex iced-wing configuration. Finally, there are numerous questions related to turbulence modeling, e.g., regions of massive separations and surface roughness.

The effort reported here had two objectives: 1) to evaluate the effectiveness of current computational fluid dynamics technology for predicting flow fields for a wing with a glaze ice accretion and 2) to investigate the effects of spanwise variation of ice shapes on the resulting computed flow fields. Steady-state solutions of the Reynolds-averaged Navier-Stokes (RANS) equations were computed using the Cobalt flow solver[9] for a constant-section, rectangular wing with an extruded two-dimensional glaze ice shape. The one-equation Spalart-Allmaras turbulence model[10] was used. The results were compared with data obtained from a recent wind tunnel test.[11,12] Two-dimensional predictions made for the same airfoil/ice accretion are presented in a second paper in this session.[13]

The basic ice shape considered was the 22.5-minute glaze ice accretion on a GLC305 airfoil, which is denoted as the two-dimensional 944 glaze ice shape.[14] The effects of spanwise variation in the ice shape on the resulting flow field were also investigated by computing flow fields for synthetic ice shapes that were generated by merging the two-dimensional ice shape with the clean wing using a sinusoidal blending function and comparing these results with clean wing and extruded wing predictions.

We first provide a description of the computational problem and present the method used to generate the synthetic ice shapes. We then briefly describe the mesh generation process and the flow solver. Finally, we present the results obtained to date.

Problem Statement

The prediction of the aerodynamic characteristics of an iced wing is a complex problem that involves several steps. In order to motivate our approach, we now provide a problem definition. Given a geometric definition of a wing with an ice accretion:

- Develop a representation of the surface that is suitable for generating a surface mesh
- Specify the artificial boundaries needed to define the computational domain, e.g., the outer boundary and the side boundaries
- Generate a mesh and specify boundary conditions on the bounding surfaces of the computational domain
- Generate a mesh in the interior of the computational domain
- Generate a flow solution

Since the wing employed for the test program was mounted between walls, the geometry modeled in this study did not include wing tips.

Geometry Modeling

We developed a technique to generate a wing with a synthetic three-dimensional ice accretion given an airfoil definition and a two-dimensional ice shape. The algorithm interpolates between the clean shape and the ice shape using a sinusoidal weighting that depends on the spanwise location.

We now describe the basic algorithm. Given a point on an airfoil with an ice accretion (x_{iced}, y_{iced}) and the point on the corresponding clean airfoil (x_{clean}, y_{clean}) definition that is closest to (x_{iced}, y_{iced}), interpolate between the iced shape and the clean shape using a factor that depends on the spanwise position

$$x_{new} = x_{clean} + (x_{iced} - x_{clean}) \times \sigma(z)$$
$$y_{new} = y_{clean} + (y_{iced} - y_{clean}) \times \sigma(z) \qquad (1)$$

where $\sigma(z)$ is defined as

$$\sigma(z) = \max\left(0.0, 1 + \frac{1}{2}\delta\left(\cos\left(2\omega\pi\frac{z}{b}\right) - 1\right)\right). \qquad (2)$$

δ is the deviation from the clean surface, z is the spanwise position, ω is the frequency of the oscillation, and b is the total wingspan. Note that the max function ensures that $\sigma(z)$ is nonnegative. The function multiplying the deviation δ varies between 0 and –2 so that the maximum value of $\sigma(z)$ is 1 and the minimum value is 1-δ with a sinusoidal variation in between. If $\sigma(z)$ is unity, the iced shape is returned. If $\sigma(z)$ is zero, the clean shape is returned. It should be noted that, for complex ice shapes, a ray extended from the clean airfoil surface in the direction of the local surface normal may intersect the ice shape more than once. The above procedure may produce a "folded" surface in this case if larger values of the deviation parameter δ are employed. The 944 glaze ice shape is one such shape.

Figure 1 shows four geometries. The "4-cycle" and "8-cycle" cases were generated using δ=0.2. These cases were selected because the resulting ice shapes exhibit spanwise variations that resemble realistic three-dimensional ice accretions. Figure 2 shows the effects of varying δ. Figures 2(a) and 2(b) show valid surfaces generated using δ=0.2 and δ=0.5, respectively. Figures 2(c) and 2(d) show invalid surfaces that are generated using δ=1.0 and δ=1.25, respectively, and are included only to show the effects of δ variation.

Mesh Generation

For each geometry, a structured surface mesh was extruded from the section description according to Eq. (1). This surface mesh was then converted to a NURBS representation using the mesh generation software GUM-B.[15] The baseline (coarse) surface and volume meshes were generated using SolidMesh. SolidMesh is an interface to the unstructured surface and volume mesh generation software AFLR2 and AFLR3.[16] AFLR3 uses an advancing front algorithm to insert a point in the mesh. The point insertion is followed by a local reconnection to improve mesh quality. The refined surface and volume meshes were generated using GridTool[17] and VGrid.[18] VGrid uses an advancing front algorithm to generate a tetrahedral volume mesh. For the all-tetrahedral meshes generated using VGrid, the near-body elements are converted into prisms producing a mixed element hybrid mesh. SolidMesh produces a hybrid mesh with prisms and tetrahedra automatically. These hybrid meshes were employed because of their potential for improved efficiency and accuracy in comparison to unstructured tetrahedral meshes. The GridTool/VGrid combination gave somewhat more user control of the point spacing than SolidMesh for the wing surface as well as in the flow field.

Table 1 shows statistics for the five meshes employed to generate the results reported here. In all cases, the distance to the first point off the wall was defined so that an average y^+ value less than 0.1 was obtained. This value is well within the recommended values for the turbulence model employed.

Figure 3 shows cross-sections through the baseline and refined meshes generated for the wing with the extruded ice shape. Note that these are cutting planes so that the line segments that appear represent intersections of faces with the cutting plane. However, the connectivity of the mesh is evident and the prism layer near the body surface is clearly visible. Also, Figure 3(a) shows the faceted surface represented by the triangular surface mesh on the extruded wing. Notice that even though the surface definition is two-dimensional, the resulting faceted surface exhibits a spanwise variation due to the unstructured nature of the mesh. Additionally, due to the manner in which the spacing is controlled in SolidMesh, there is a spanwise variation in the spacing. The volume mesh in the region downstream of the upper horn is relatively coarse. Refining the surface mesh reduces the faceting and improves the mesh density in the region where flow separation is anticipated as shown in Figure 3(b). Additionally, a more uniform distribution of edge lengths is obtained over the surface using the GridTool/VGrid combination.

	# Nodes	# Faces	# Cells
Clean wing	630,285	4,711,884	2,150,999
Extruded wing (baseline)	890,958	5,299,738	2,258,447
Extruded wing (refined)	1,828,711	17,327,367	8,341,019
4-Cycle wing (δ=0.2)	904,680	5,368,010	2,285,734
8-Cycle wing (δ=0.2)	903,654	5,360,055	2,281,964

Table 1. Statistics for meshes employed in this effort.

Flow Solution

The flow solver employed in this effort is the noncommercial version of Cobalt.[9] The Cobalt flow solver was designed for general unstructured meshes. It employs a nonlinear Riemann solver for the inviscid flux computations and can be run either in explicit or implicit mode. In all cases reported here, the solution to the RANS equations was obtained using first-order, implicit local time stepping and does not in any way represent a time-accurate solution. Second-order spatial accuracy was obtained using a linear least-squares reconstruction of the data. Several turbulence models are available including the Spalart-Almaras one-equation model[10] that was used for the computations reported here. A slip boundary condition was applied on the artificial side boundaries.

Results

In this section we present a comparison of predicted steady RANS results with experimental data[11,12] for the rectangular business jet wing with the extruded 944 glaze ice shape. We also include a brief discussion on the effects of spanwise variation of the ice shape.

We computed steady RANS solutions using the Cobalt flow solver with the Spalart-Allmaras turbulence model

Figure 1(a). Clean GLC305 wing section

Figure 1(b). Extruded 944 glaze ice wing section

Figure 1(c). "4-cycle" wing section
δ=0.2, ω=4

Figure 1(d). "8-cycle" wing section
δ=0.2, ω=8

Figure 1. Iced wing configurations demonstrating the effects of ω variation

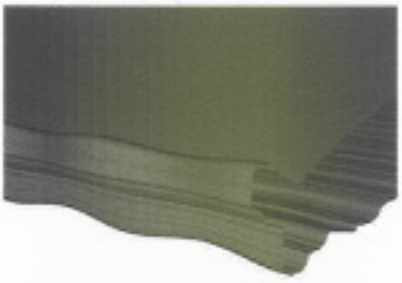

Figure 2(a). "8-cycle" wing section
δ=0.2, ω=8

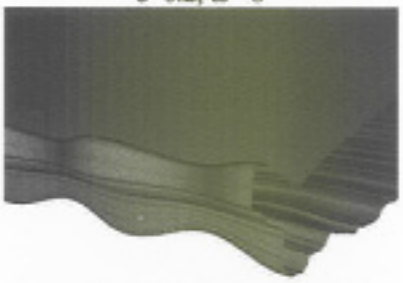

Figure 2(b). "8-cycle" wing section
δ=0.5, ω=8

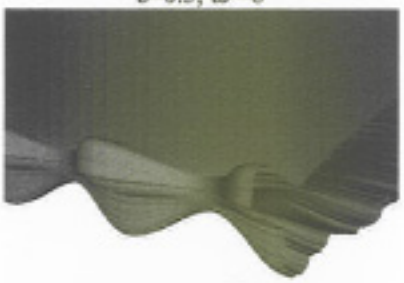

Figure 2(c). "8-cycle" wing section
δ=1.0, ω=8

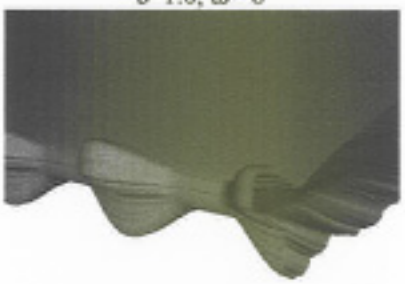

Figure 2(d). "8-cycle" wing section
δ=1.25, ω=8

Figure 2. Effect of δ variation on resulting wing shape. Figures 2(c) and 2(d) represent invalid geometries due to surface "folding."

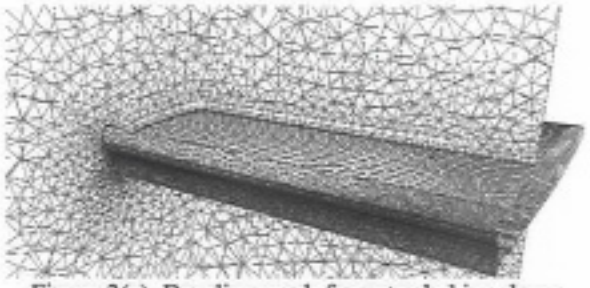

Figure 3(a). Baseline mesh for extruded ice shape

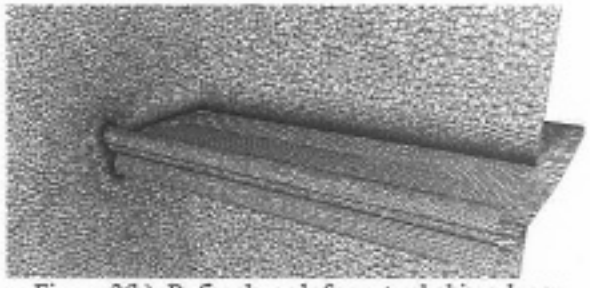

Figure 3(b). Refined mesh for extruded ice shape

Figure 3. Mesh in cutting plane for extruded 944 glaze ice shape – (a) baseline mesh and (b) refined mesh

for the following conditions: M=0.12, Re/L=3.8x10^6/m which, with a chord length of 0.9144m, yields Re=3.5x10^6, and angles of attack of 0°, 2°, 4°, and 6°. The clean GLC305 wing cases correspond to Run 9 in the experimental data. The extruded 944 ice shape cases correspond to Run 41.

All cases reported below were run on 64 processors on the EMPIRE cluster at the ERC at Mississippi State University. The EMPIRE cluster is a supercomputer-class cluster of workstations consisting of 1038 one-GHz or better Pentium III processors each with one or more GB of RAM. Solutions computed on the baseline mesh for the extruded wing required approximately 4 CPU hours per thousand time steps. Solutions computed on the refined mesh for the extruded wing configuration required approximately 16 CPU hours per thousand time steps.

Clean Wing: Comparison with Experimental Data

For the purposes of establishing a baseline level of confidence for the methodology employed here, we first compare predicted results with experimental data for the clean wing, i.e., a rectangular wing with the GLC305 section and an aspect ratio of unity.

The first point to consider is the convergence of the solution. Figure 4 shows several convergence measures for the 6° angle of attack computation. It is representative of the other computations. Figure 4(a) shows the the L_2 norm of the residual. The residual decreases slightly more than one order of magnitude during the computation. Figures 4(b) and 4(c) show the lift and axial force histories, respectively. Notice that in both cases, the solution appears to have reached a steady state.

Figure 5 shows comparisons of computed results with experimental data. Figure 5(a) shows a comparison of the predicted and experimental lift coefficients obtained by integrating the surface pressures. In this case, there is excellent agreement between the predicted results and the experimental data. This is to be expected for these relatively low angle of attack cases. Figure 5(b) shows a comparison of predicted and experimental drag curves. The drag coefficient was obtained for the prediction by integrating the pressure and the viscous stresses over the surface of the airfoil. The experimental drag force coefficient was obtained by integrating a wake survey. In this case, the data does not show agreement similar to that obtained for the lift results. This occurs because, for the streamlined body under consideration at low angle of attack, the drag is primarily due to viscous stresses. Finally, Figure 5(c) shows a comparison of the predicted and experimental pressure coefficients at an angle of attack of 6°. As suggested by the lift curves, the agreement between the prediction and experiment is very good. There was little spanwise variation in the computed surface pressures.

Extruded Wing: Comparison with Experimental Data

We now compare results computed for the extruded wing based on the two-dimensional 944 glaze ice shape.[14] Computations were performed on the meshes denoted as "extruded wing (baseline)" and "extruded wing (refined)" in Table 1.

Figure 6 shows the convergence histories for the extruded wing computation for an angle of attack of 6° using the baseline mesh. The L_2 residual, the lift force, and the axial force reached asymptotic values as shown in Figures 6(a), 6(b), and 6(c), respectively. This computation is representative of the computations for other angles of attack using this mesh.

Figure 7 shows the convergence histories for the extruded wing computation for an angle of attack of 6° using the refined mesh. Figure 7(a) shows that the L_2 residual has reached an asypmtotic value. The lift force and axial force have also reached asymptotic values as shown in Figures 7(b) and 7(c), respectively. This convergence history is representative of the computations for other angles of attack using this mesh.

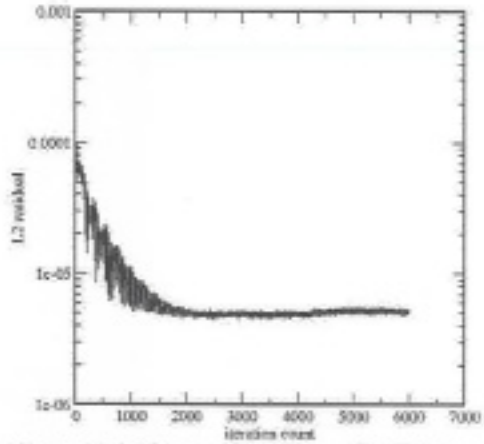

Figure 4(a). Clean wing – L_2 residual history

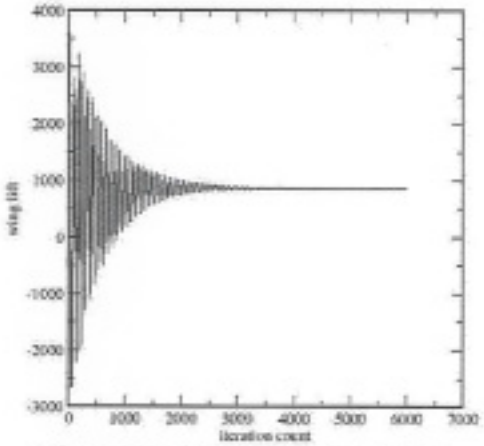

Figure 4 (b). Clean wing – lift history

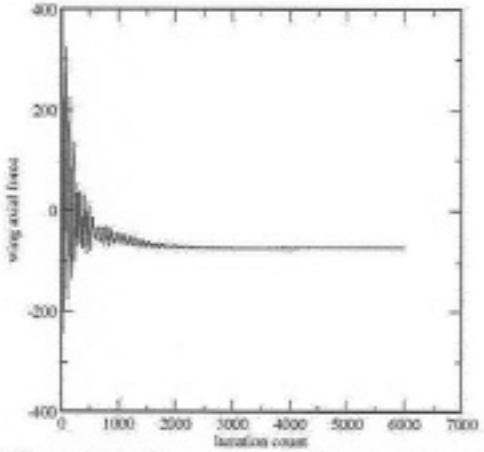

Figure 4(c). Clean wing – axial force history

Figure 4. Convergence of clean GLC305 wing computation – α=6°

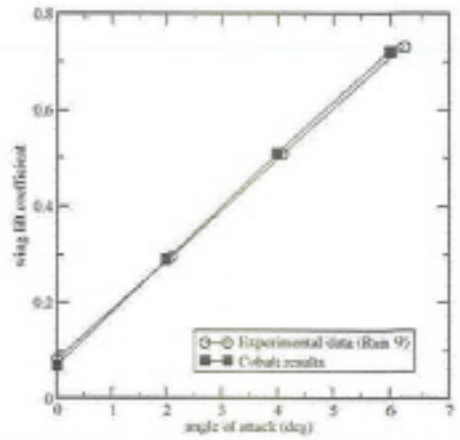

Figure 5(a). Clean wing – lift coefficient vs. angle of attack

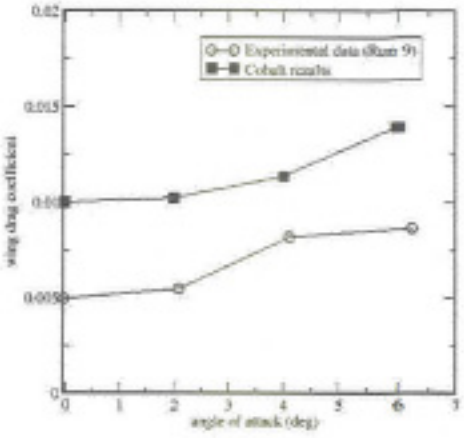

Figure 5(b). Clean wing – drag coefficient vs. angle of attack

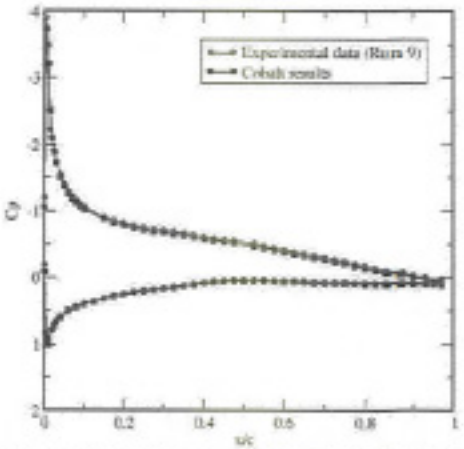

Figure 5(c). Clean wing – chordwise distribution of pressure coefficient – α=6° (midspan)

Figure 5. Comparison of predicted results with experimental data for the extruded GLC305 wing

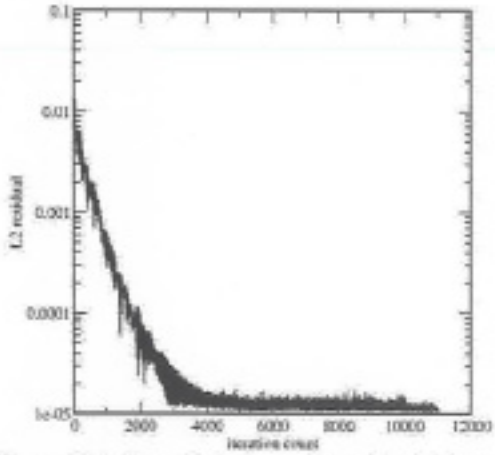

Figure 6(a). Extruded wing – L_2 residual history (baseline mesh)

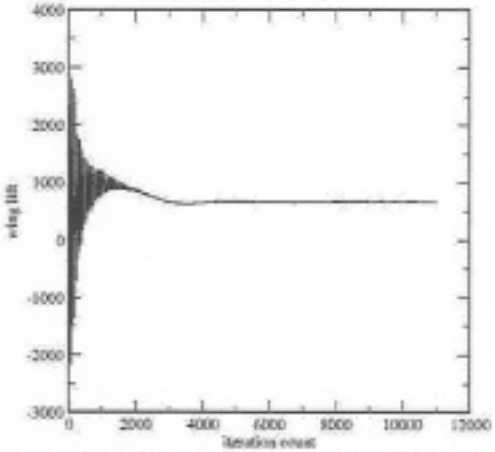

Figure 6(b). Extruded wing – wing lift history (baseline mesh)

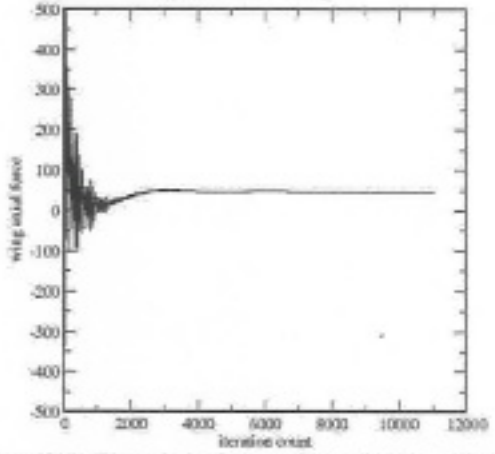

Figure 6(c). Extruded wing – wing axial force history (baseline mesh)

Figure 6. Convergence of extruded 944 glaze ice shape computation – α=6° (baseline mesh)

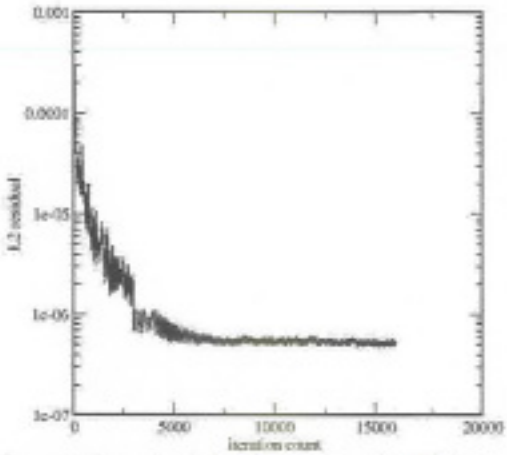

Figure 7(a). Extruded wing – L_2 residual history (refined mesh)

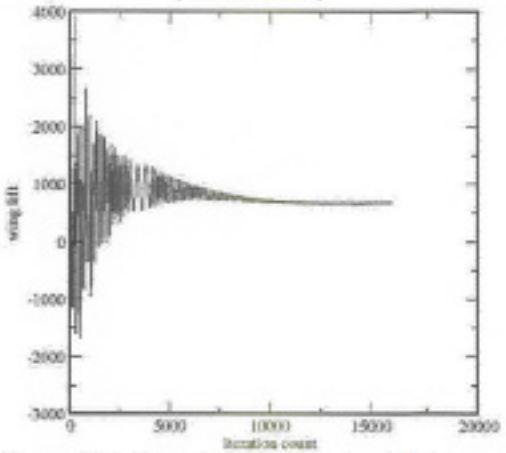

Figure 7(b). Extruded wing – wing lift history (refined mesh)

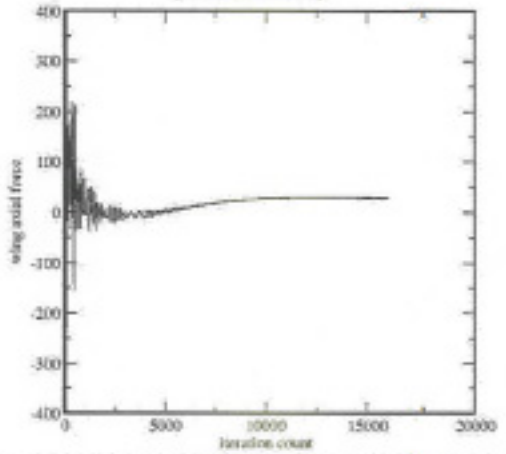

Figure 7(c). Extruded wing – wing axial force history (refined mesh)

Figure 7. Convergence of extruded 944 glaze ice shape computation – α=6° (refined mesh)

Figure 8 shows a comparison of the wing lift and drag coefficients predicted using the baseline mesh and the refined mesh with experimental data for an angle of attack range of 0° to 6° in 2° increments. As shown in Figure 8(a), the lift coefficient at 0° is well predicted. However, as the angle of attack is increased, the lift is underpredicted relative to the experimental data. Addititionally, the break in the predicted lift curve slope is characteristic of the "near stall" behavior of the wing suggesting that the predictions are overestimating the extent of the flow separation. On the other hand, as shown in Figure 8(b), the predicted drag coefficient shows very good agreement with the experimental data. This agreement can be attributed to the fact that the drag is primarily composed of form or pressure drag for this configuration, i.e., the ice shape is a bluff body. However, the very good agreement between the results predicted using the baseline mesh and the experimental data appears to be fortuitous. The agreement is not as good for predictions made using the refined mesh. It should be noted that, for each case considered, there are only very slight spanwise variations in the pressure distribution.

Figure 9 shows a comparison of the predicted midspan pressure coefficients for the baseline mesh and the refined mesh and experimental data for an angle of attack range of 0° to 6° in 2° increments. For the most part, the lower surface pressures are well predicted using either the baseline mesh or the refined mesh. The differences in the predicted upper surface pressure coefficients are consistent with those in the lift coefficients. Mesh refinement improves agreement with the experimental data somewhat and indicates a strengthened recirculation region. These results suggests that further mesh refinement may be neccesary. However, it may be that a steady RANS solution will not accurately capture the recirculating region and an alternative procedure such as an unsteady Detatched Eddy simulation (DES)[19] may be necessary for this case. These results are consistent with those reported by Chi, et. al.[13]

We now include a detailed comparison of computed flow field velocities (the u-component of the velocity) with experimental data obtained using the split-film technique as reported by Broeren, et al.[12] The split-film technique is a variation of hot-wire anemometry. Metallic films are deposited on opposite sides of a small cylinder. The cylinder is then placed perpendicular to the primary flow direction of interest and heated using an electric current. By monitoring the voltages needed to maintain constant current, the magnitude and direction of flow in the primary direction, u, can be determined. The magnitude of the v-component of velocity may also be ascertained, but not its direction. We do not include any comparisons with the v-component and, since our results are steady RANS computations, we consider comparisons only time-averaged mean flow values.

Figures 10-12 show comparisons of the predicted u-component of velocity with experimental data for both the baseline mesh and the refined mesh for angles of attack of 0°, 4°, and 6°. It should be noted that the color scales employed to display the predicted data and the experimental data are somewhat different. Using these images, the reattachment location of the primary upper surface flow separation may be estimated by locating the position on the chord at which the contour u=0 intersects the upper surface of the wing. The general trend exhibited in these images is that, at an angle of attack of 0°, the reattachment position is well predicted using either the baseline mesh or the refined mesh. However, as the angle of attack increases, the extent of the separated region is overpredicted until the flow is completely separated on the upper surface at an angle of attack of 6°. Mesh refinement does improve the prediction relative to the baseline mesh. However, the extent of the separated region is still overestimated. The extra dissipation present in the baseline mesh solution is evident from the increased spreading of the shear layer in comparison to results predicted using the refined mesh. However, this spreading is not as severe as expected given the relative coarseness of the baseline mesh. The seemingly anomalous velocity contours that appear in the experimental data just downstream of the horn are artifacts from the process employed to generate the contour plots.

Figures 13 and 14 show predictions of separation (red) and attachment (blue) locations for an angle of attack range of 0° to 6° in 2° increments for the baseline mesh and the refined mesh, respectively. The technique of Kenwright[20] is employed to locate surface mesh elements in which a potential separation or attachment line crosses. No attempt is made here to reconstruct the actual curves. Kenwright's technique is based on a phase plane analysis of critical points in the velocity field "close" to the surface and, as such, is subject to anomalous results if there is "noise" in the data.

The refined mesh results show fairly well resolved flow features including secondary chordwise separations and corresponding attachments clearly indicated just down stream of the horn (the closely spaced, roughly parallel blue and red curves located just aft of the leading edge). The refined mesh results show a relatively uniform primary reattachment across the span in each case. The baseline mesh does not resolve this secondary separation at any angle of attack. Additionally, the location of the primary reattachment predicted using

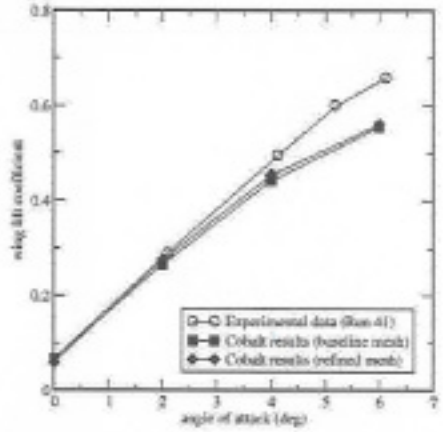

Figure 8(a). Extruded wing – lift coefficient vs. angle of attack

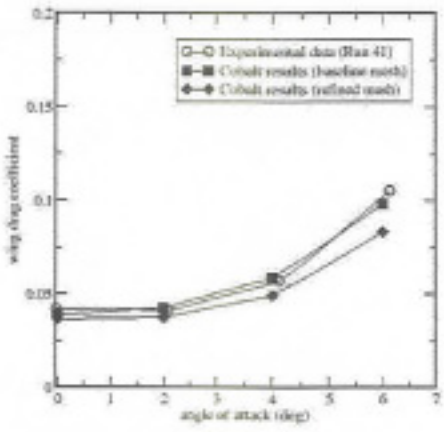

Figure 8(b). Extruded wing – drag coefficient vs. angle of attack

Figure 8. Comparison of predicted force coefficients with experimental data for the extruded 944 glaze ice shape (baseline mesh and refined mesh)

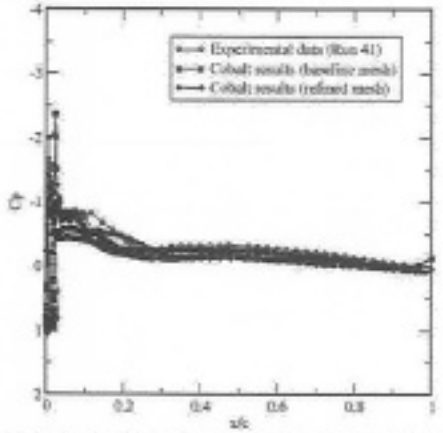

Figure 9(a). Extruded wing pressure distribution – α=0°

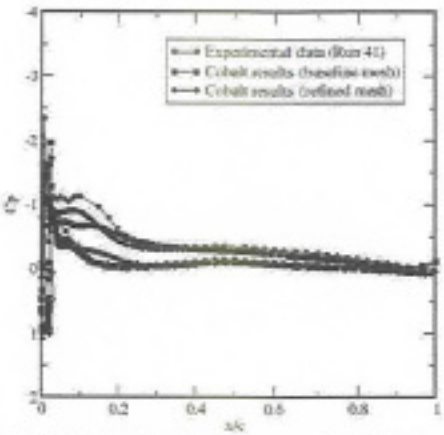

Figure 9(b). Extruded wing pressure distribution – α=2°

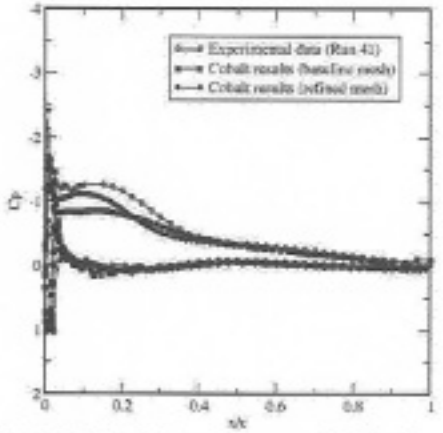

Figure 9(c). Extruded wing pressure distribution – α=4°

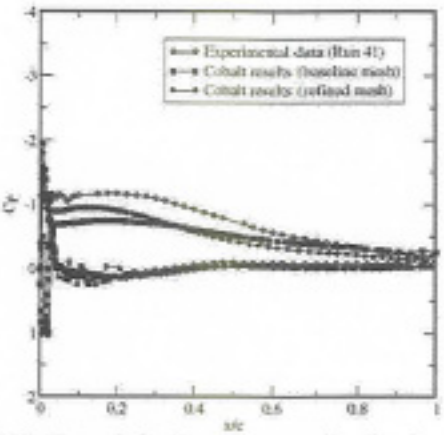

Figure 9(d). Extruded wing pressure distribution – α=6°

Figure 9. Comparison of predicted pressure coefficients (midspan) with experimental data for the extruded 944 glaze ice shape (baseline mesh and refined mesh)

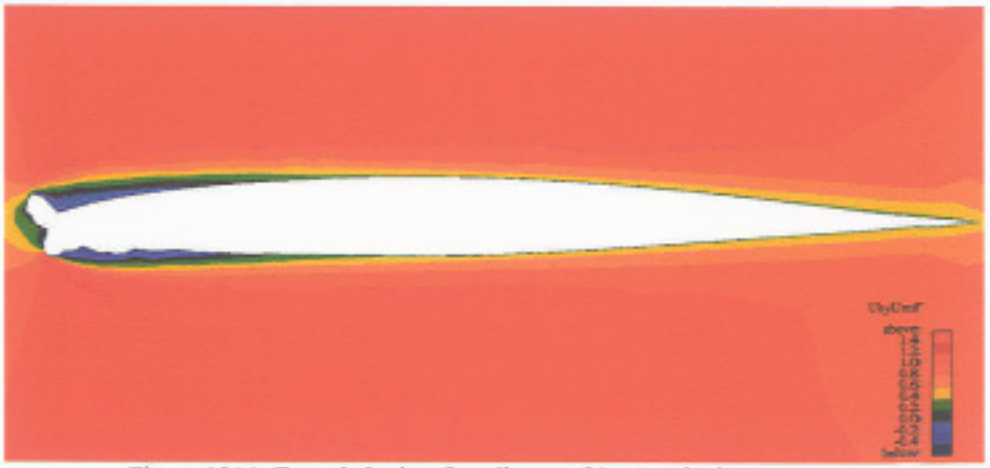

Figure 10(a). Extruded wing (baseline mesh) – u-velocity contours

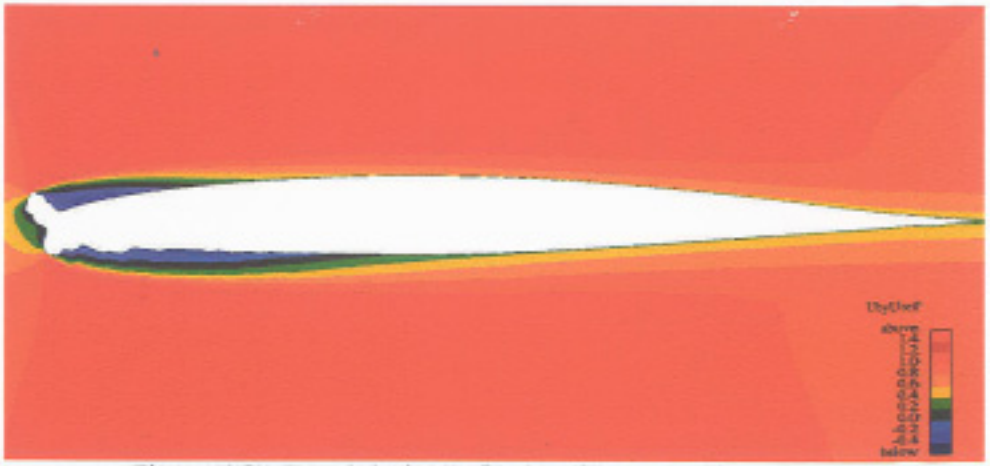

Figure 10(b). Extruded wing (refined mesh) – u-velocity contours

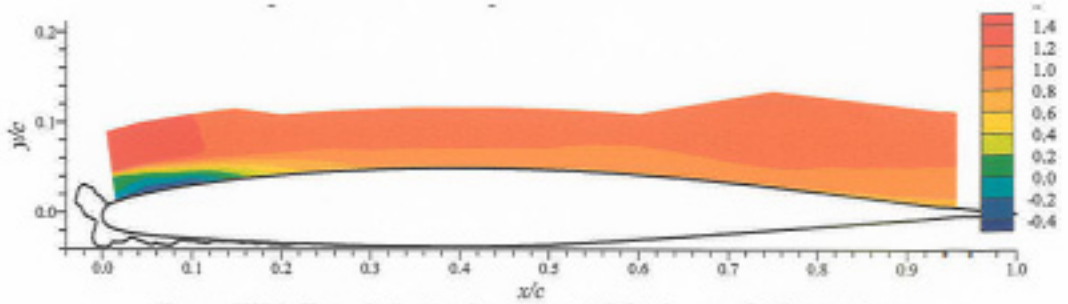

Figure 10(c). Extruded wing (experimental data) – u-velocity contours

Figure 10. Comparison of predicted u-velocity contours (midspan) with experimental data for the extruded 944 glaze ice shape (baseline mesh and refined mesh) – $\alpha = 0°$

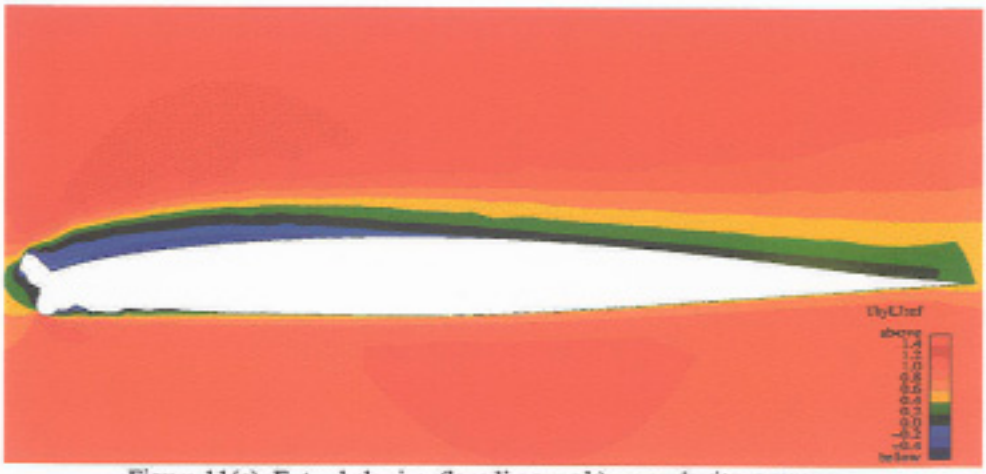

Figure 11(a). Extruded wing (baseline mesh) – u-velocity contours

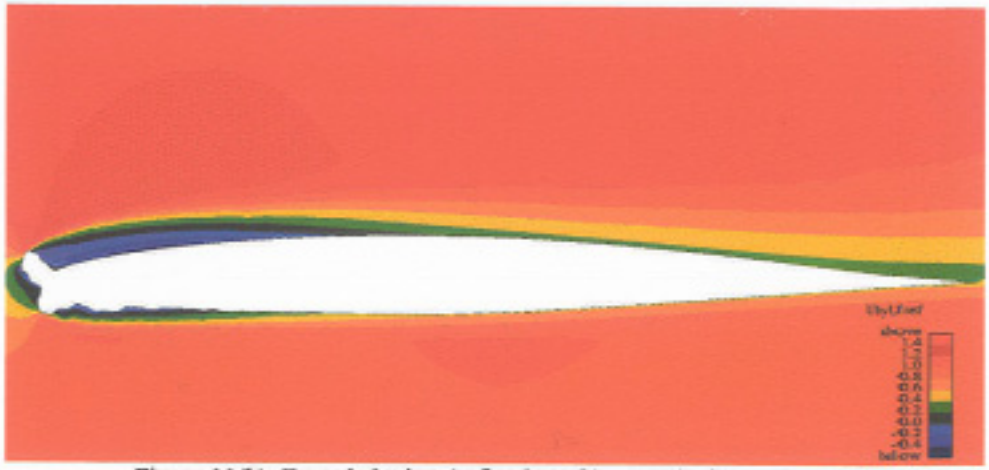

Figure 11(b). Extruded wing (refined mesh) – u-velocity contours

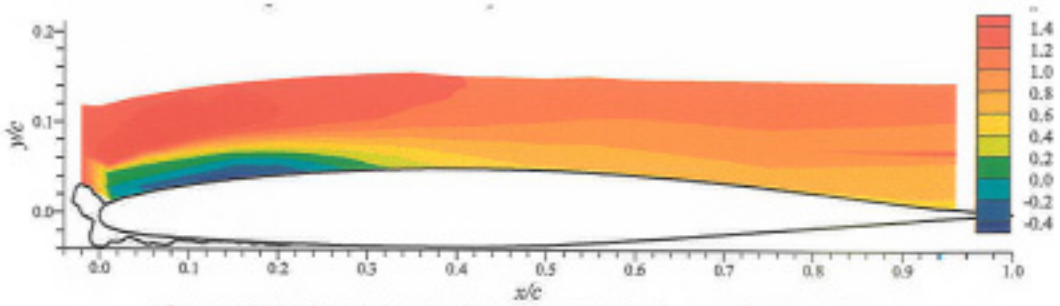

Figure 11(c). Extruded wing (experimental data) – u-velocity contours

Figure 11. Comparison of predicted u-velocity contours (midspan) with experimental data for the extruded 944 glaze ice shape (baseline mesh and refined mesh) – α=4°

Figure 12(a). Extruded wing (baseline mesh) – u-velocity contours

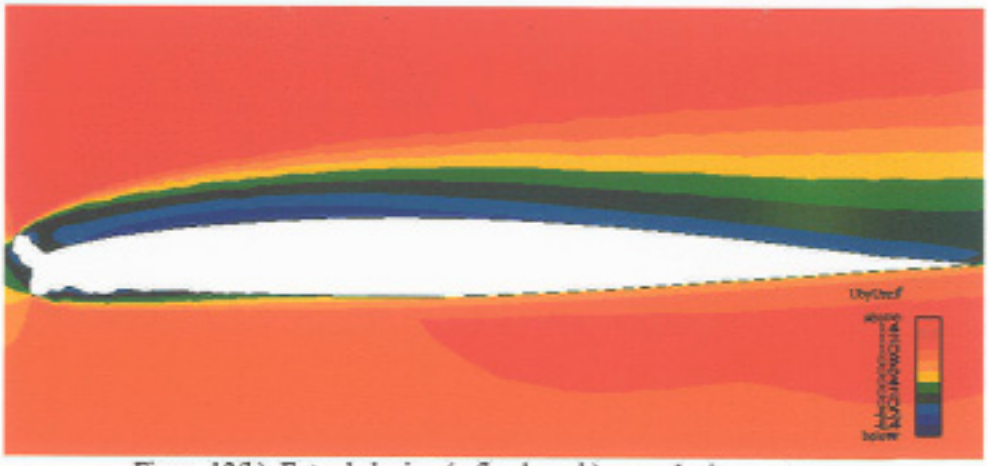

Figure 12(b). Extruded wing (refined mesh) – u-velocity contours

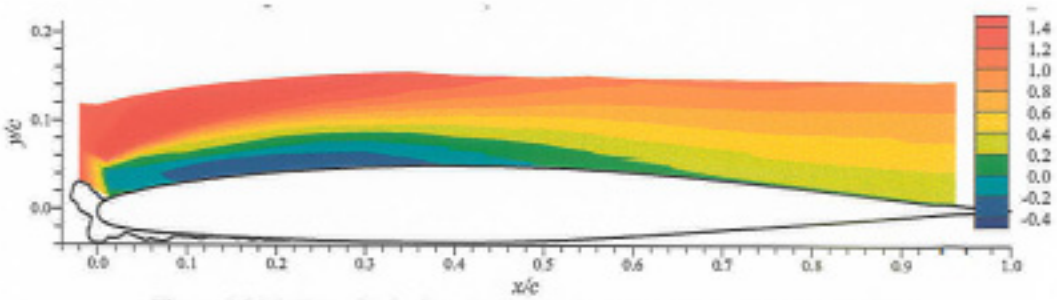

Figure 12(c). Extruded wing (experimental data) – u-velocity contours

Figure 12. Comparison of predicted u-velocity contours (midspan) with experimental data for the extruded 944 glaze ice shape (baseline mesh and refined mesh) – α=6°

Figure 13(a). Upper surface separation and reattachment lines (left) and streamline traces (right) – α=0°

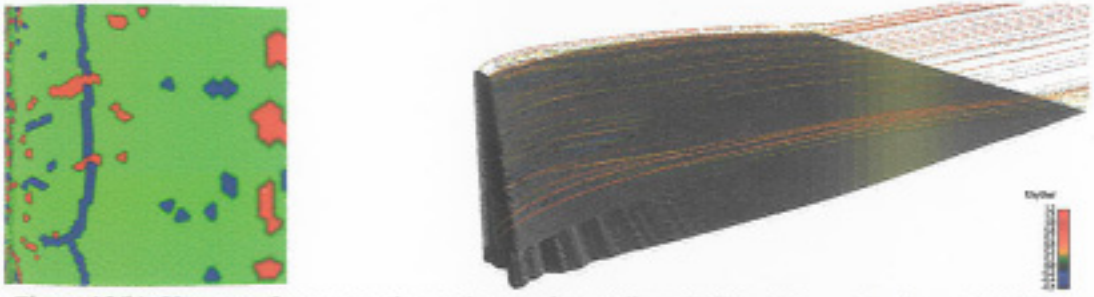

Figure 13(b). Upper surface separation and reattachment lines (left) and streamline traces (right) – α=2°

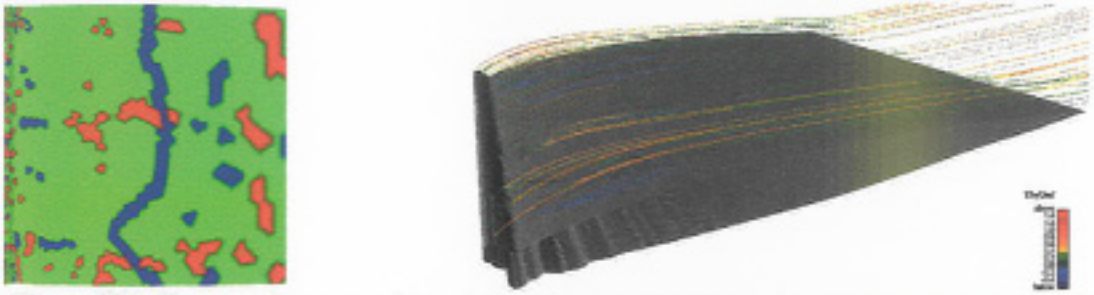

Figure 13(c). Upper surface separation and reattachment lines (left) and streamline traces (right) – α=4°

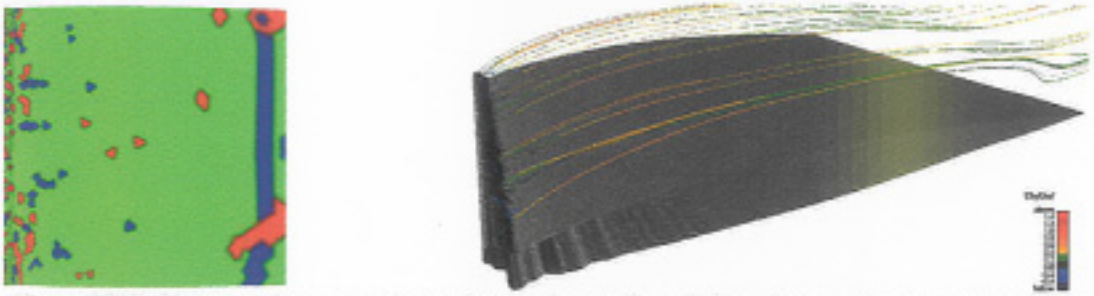

Figure 13(d). Upper surface separation and reattachment lines (left) and streamline traces (right) – α=6°

Figure 13. Predicted upper surface separation (red) and attachment (blue) lines and streamline traces colored by the u-component of velocity – extruded 944 glaze ice shape (baseline mesh)

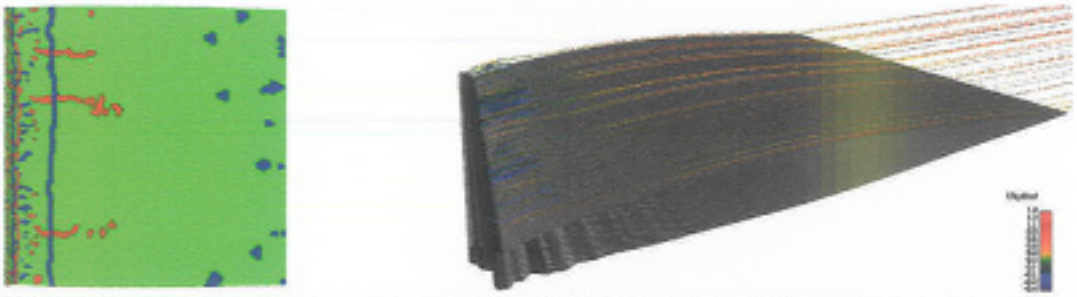

Figure 14(a). Upper surface separation and reattachment lines (left) and streamline traces (right) – α=0°

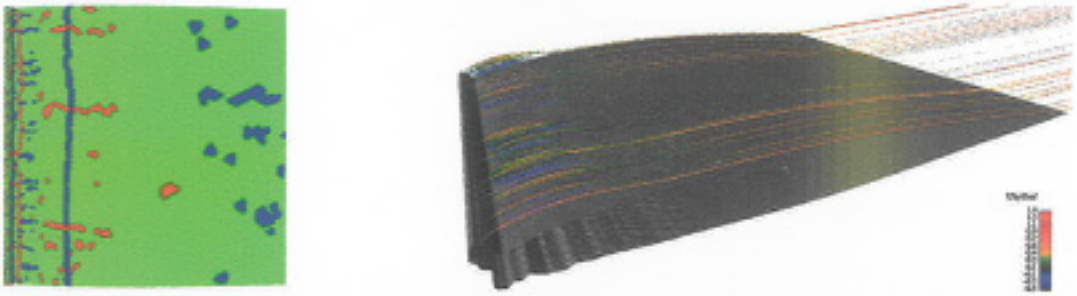

Figure 14(b). Upper surface separation and reattachment lines (left) and streamline traces (right) – α=2°

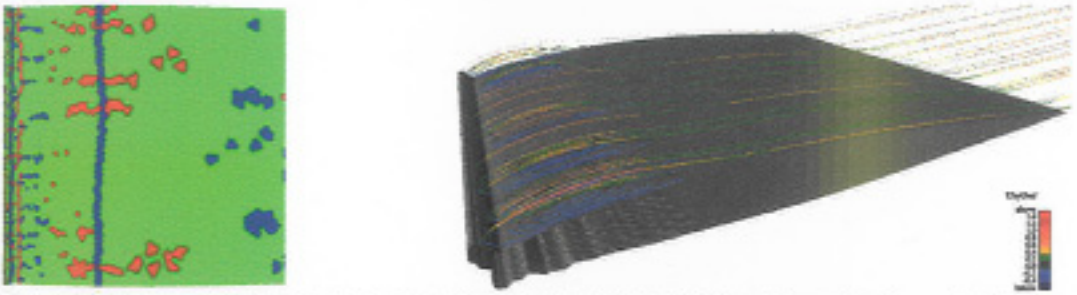

Figure 14(c). Upper surface separation and reattachment lines (left) and streamline traces (right) – α=4°

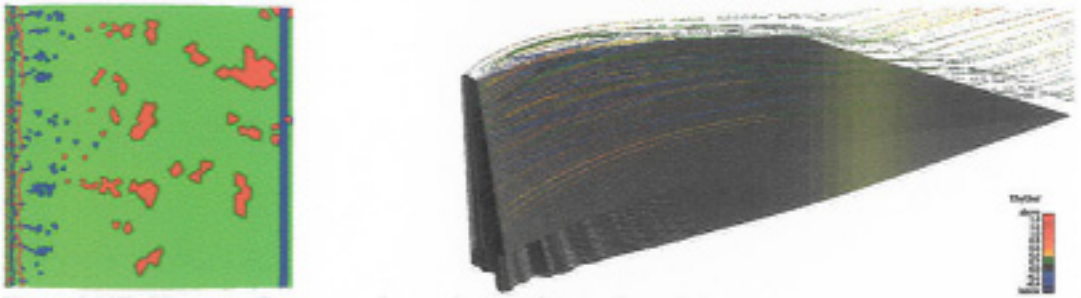

Figure 14(d). Upper surface separation and reattachment lines (left) and streamline traces (right) – α=6°

Figure 14. Predicted upper surface separation (red) and attachment (blue) lines and streamline traces colored by the u-component of velocity – extruded 944 glaze ice shape (refined mesh)

does not exhibit the same uniformity that is present in the refined mesh computations except for the 6° case which is fully separated. We suggest that the coarser, nonuniform surface mesh employed in the baseline mesh (see Figure 3(a)) is responsible for the apparent nonuniformity of the baseline mesh flow fields. Conclusions drawn regarding the attachment locations are consistent with those drawn from the velocity contours for the 0°, 4°, and 6° cases.

Also shown in Figures 13 and 14 are instantaneous streamlines at each angle of attack for both meshes. The nonuniformity in the baseline mesh flow field is also evident in the streamlines. At each angle of attack, the streamline traces for the baseline mesh solution show considerably more three-dimensional behavior than the streamline traces for the refined mesh solution. However, we do not suggest that the baseline mesh more accurately models an iced wing flow field. The random faceting, which occurs because of the orientation of the surface triangles, appears at the highest frequency representable by the mesh. Although the faceting of the surface shown in Figure 3(a) does more closely resemble an iced wing surface than the smoother description shown in Figure 3(b), the flow features associated with this faceting would not be resolved on this mesh. It is difficult to state conclusively that the chordwise curves represent real features in the data. It is likely that they represent inadequately resolved secondary flow features. Additionally, the predicted results show that once the flow becomes fully separated, these secondary structures lose their coherence.

It should be noted that, although the details of the flow field were not well predicted using the baseline mesh, the predictions appear to be conservative. That is, the lift degradation predicted by the baseline mesh solutions is more severe than the experimental data. The is primarily due to the more extensive flow separation predicted using the baseline mesh.

Effects of Spanwise Variation

We now consider the effects of spanwise variation in the ice shape. The configurations employed here are the four configurations shown in Figure 1 – the clean GLC305 wing, the extruded 944 glaze ice shape, the "4-cycle" wing, and the "8-cycle" wing. The 4-cycle and 8-cycle cases with δ=0.2 represent reasonable three-dimensional ice shapes. The meshes for these cases, described in Table 1, are roughly equivalent, in resolution, to the baseline mesh for the extruded wing.

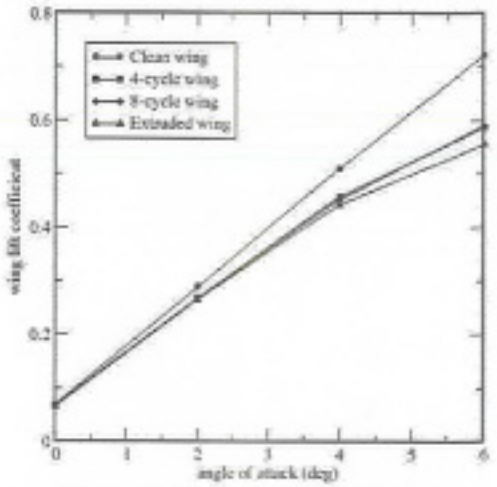

Figure 15(a). Wing lift coefficient

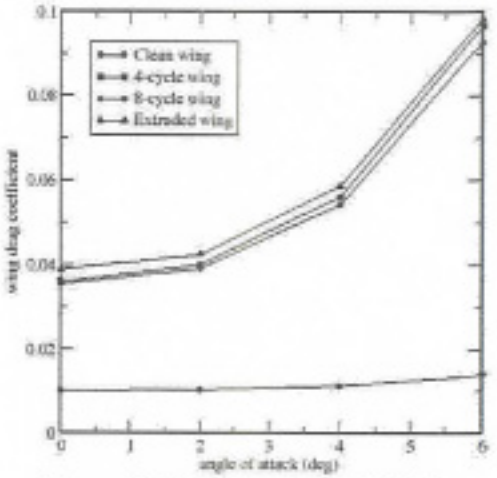

Figure 15(b). Wing drag coefficient

Figure 15. Comparison of predicted wing lift and drag coefficients for four different configurations – clean GLC305 wing, extruded 944 glaze ice shape (baseline mesh), 4-cycle wing with δ=0.2, and 8-cycle wing with δ=0.2

Figure 15 shows a comparison of the lift and drag coefficients predicted for each of the four configurations across an angle of attack range of 0° to 6° in 2° increments. Of significance here is the fact that the clean wing and extruded wing bound both the lift and drag behavior of the other configurations. This implies that the extruded wing provides a conservative estimate for the predicted lift and drag. On the surface, this result appears reasonable since the spanwise variation in the ice shape effectively lessens the volume of the accreted ice and produces a smaller blockage effect. However, this conclusion has not been substantiated for other configurations and should not be extrapolated at this time.

Figures 16 and 17 show predictions of separation (red) and attachment (blue) locations for an angle of attack range of 0° to 6° in 2° increments for the 4-cycle wing and the 8-cycle wing, respectively. In general, the results indicate the presence of secondary structures that are introduced by the spanwise variation in the ice shape. The structures interact with the flow field to produce an irregular primary reattachment region. Not surprisingly, there is a quasi-periodic variation that appears to be associated with the spanwise variation of the ice shape. It should be noted that these secondary structures are not adequately resolved on these meshes. Also included in Figures 16 and 17 are the instantaneous streamlines for each angle of attack. As expected, the streamlines show considerable three-dimensional flow. The streamlines indicate the presence of complex flow patterns in the region just downstream of the horn, even at the lower angles of attack. However, the spanwise flow does not appear to significantly alter the global characteristics of the flow field. In particular, although the overall shape of the primary reattachment varies between Figures 13 (extruded 944 glaze ice shape), 16 (4-cycle wing), and 17 (8-cycle wing), its location is essentially unaltered.

Conclusions

The results computed as part of this effort indicate that the steady RANS solutions do not accurately capture the recirculating region downstream of the 944 glaze ice accretion, even after a mesh refinement, and that the resulting predicted reattachment is farther downstream than that indicated by the experimental data. Additionally, the detailed flow characteristics in the solutions computed on the coarse, baseline mesh were different than those computed on the refined mesh. It should be noted that the results presented here do not really represent a grid sensitivity study since grid independence of the solution has not been demonstrated. However, while the detailed flow characteristics on the two meshes were different, the wing lift values for the two meshes are quite similar. Further, the results predicted using the baseline mesh were conservative in the sense that they indicated a more severe reduction in lift than the experimental data.

A spanwise variation in ice shape was obtained by developing a blending function that merged the 944 glaze ice shape with the GLC305 clean section using a sinusoidal spanwise variation. Limited results indicate that, for this case, the results predicted by the extruded shape provide conservative estimates for the performance degradation of the wing. Additionally, the spanwise variation in the ice shape and the resulting differences in the flow field details did not significantly change the location of the primary reattachment. These results suggest the influence of moderate spanwise variation in the ice accretion may be only minor for gross quantities such as lift and drag.

The results reported in this paper indicate that the agreement between computed results and experimental data is degraded for cases with large regions of upper surface flow separation and are consistent with those reported for two-dimensional computations.[13] These results suggest that further refinement may be needed or that an alternative approach, such as unsteady DES, may be necessary and that further study of these issues is warranted.

Acknowledgements

The partial support of the first three authors by NASA GRC under grant NAG3-2562, Yung Choo Technical Monitor, is gratefully acknowledged. We would also like to extend our appreciation to Stuart Pope of NASA LRC for his assistance with GridTool. We would also like to thank Matthew Grismer of AFRL for his assistance with the Cobalt flow solver.

References

1. Y. Choo, K. D. Lee, D. S. Thompson, and M. Vickerman, "Geometry Modeling and Grid Generation for "Icing Effects" and "Ice Accretion" Simulations on Airfoils," Proceedings of the 7th International Conference on Numerical Grid Generation in Computational Field Simulations, Whistler, B.C., pp. 1061-1070, 2000.
2. W. B. Wright, "Users Manual for the NASA Lewis Ice Accretion Code LEWICE 2.0," NASA CR-1999-209409, September 1999.
3. J. Chung, Y. Choo, A. Reehorst, M. Potapczuk, and J. Slater, "Navier-Stokes Analysis of the Flowfield Characteristics of an Ice Contaminated Aircraft Wing," AIAA Paper 1999-0375, Presented at the 37th Aerospace Sciences Meeting and Exhibit, Reno, NV, January 1999.
4. T. Dunn and E. Loth, "Effects of Simulated-Spanwise-Ice Shapes on Airfoils: Computational Investigation," AIAA Paper 1999-0093, Presented at the 37th Aerospace Sciences Meeting and Exhibit, Reno, NV, January 1999.
5. T. Dunn, E. Loth, and M. Bragg, "Computational Investigation of Simulated Large-Droplet Ice Shapes on Airfoil Aerodynamics," *J. Aircraft*, vol. 36, pp. 836-843, 1999.
6. S. Kumar and E. Loth, "Aerodynamic Simulations of Airfoils with Upper-Surface Ice-Shapes," *J. Aircraft*, vol. 38, pp. 285-295, 2001.

Figure 16(a). Upper surface separation and reattachment lines (left) and streamline traces (right) – α=0°

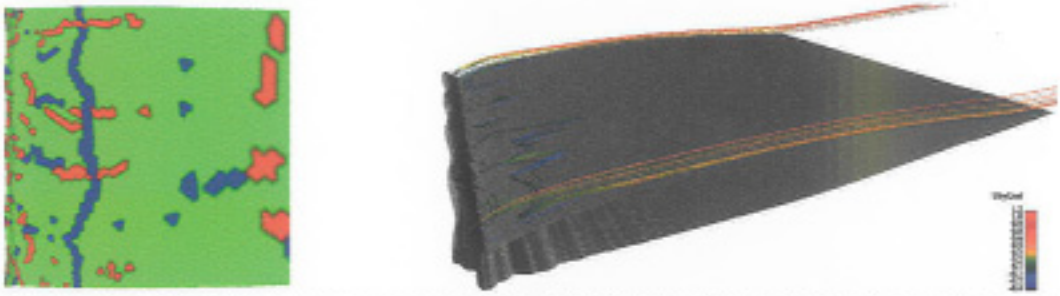

Figure 16(b). Upper surface separation and reattachment lines (left) and streamline traces (right) – α=2°

Figure 16(c). Upper surface separation and reattachment lines (left) and streamline traces (right) – α=4°

Figure 16(d). Upper surface separation and reattachment lines (left) and streamline traces (right) – α=6°

Figure 16. Predicted upper surface separation (red) and attachment (blue) lines and streamline traces colored by the u-component of velocity – 4-cycle wing with δ=0.2

Figure 17(a). Upper surface separation and reattachment lines (left) and streamline traces (right) – α=0°

Figure 17(b). Upper surface separation and reattachment lines (left) and streamline traces (right) – α=2°

Figure 17(c). Upper surface separation and reattachment lines (left) and streamline traces (right) – α=4°

Figure 17(d). Upper surface separation and reattachment lines (left) and streamline traces (right) – α=6°

Figure 17. Predicted upper surface separation (red) and attachment (blue) lines and streamline traces colored by the u-component of velocity – 8-cycle wing with δ=0.2

7. J. Pan, E. Loth, and M. Bragg, "RANS Simulations of Airfoils with Ice Shapes," AIAA Paper 2003-0729, Presented at the 41st Aerospace Sciences Meeting and Exhibit, Reno, NV, January 2003.
8. S. Kumar and E. Loth, "Detached Eddy Simulations of an Iced-Airfoil," AIAA Paper 2001-0678, Presented at the 39th Aerospace Sciences Meeting and Exhibit, Reno, NV, January 2001.
9. R. F. Tomaro, W. Z. Strang, and L. N. Sankar, "An Implicit Algorithm for Solving Time Dependent Flows on Unstructured Meshes," AIAA Paper 97-0333, Presented at 35th Aerospace Sciences Meeting and Exhibit, Reno, NV, January 1997.
10. P. R. Spalart and S. R. Allmaras, "A One-Equation Turbulence Model for Aerodynamic Flows," *La Recherche Aerospatiale*, vol. 1, pp. 5-21, 1994.
11. H. Addy, J. Zoeckler, A. Broeren, "A Wind Tunnel Study of Icing Effects on a Business Jet Airfoil," AIAA Paper 2003-0727, Presented at the 41st Aerospace Sciences Meeting and Exhibit, Reno, NV, January 6-9, 2003.
12. A. Broeren, H. Addy, and M. Bragg, "Flowfield Measurements About an Airfoil with Leading-edge Ice Shapes," AIAA Paper 2004-0559, Presented at the 42nd Aerospace Sciences Meeting and Exhibit, Reno, NV, January 2004.
13. X. Chi, B. Zhu, T. I-P. Shih, H. E. Addy, and Y. K. Choo, "CFD Analysis of the Aerodynamics of a Business-Jet Airfoil with 2-D Ice Accretion," AIAA Paper 2004-0560, Presented at the 42nd Aerospace Sciences Meeting and Exhibit, Reno, NV, January 2004.
14. H. Addy, "Ice Accretions and Icing Effects for Modern Airfoils," NASA TP-2000-210031, April 2000.
15. M. Jiang and M. Remotigue, "GUM-B Grid Generation Code and Applications," Numerical Grid Generation in Computational Field Simulations, Proceedings of the 6th International Conference, London, England, July 1998.
16. D. Marcum, "Unstructured Grid Generation using Automatic Point Insertion and Local Reconnection," *Handbook of Grid Generation*, J. F. Thompson, B. K. Soni, and N. Weatherill, eds, CRC Press, Boca Raton, FL, 1998.
17. J. Samareh, "GridTool: A Surface Modeling and Grid Generation Tool," Proceedings of the Workshop on Surface Modeling, Grid Generation, and Related Issues in CFD Solutions, NASA CP-3291, May 1995.
18. S. Pirzadeh, "Three-Dimensional Unstructured Viscous Grids by the Advancing Layers Method," *AIAA Journal*, Vol. 34, No. 1, January 1996, pp. 43-49.
19. M. Strelets, "Detached Eddy Simulation of Massively Separated flows," AIAA Paper 2001-0879, Presented at 39th Aerospace Sciences Meeting and Exhibit, Reno, NV, January 2001.
20. D. Kenwright, "Automatic Detection of Open and Closed Separation and Attachment Lines," *Proc. Visualization '98*, pp. 151-158, 1998.